Characterization of an x-ray-flux source for the production of high-energy-density plasmas

D. R. Kania, H. Kornblum, and B. A. Hammel
Lawrence Livermore National Laboratory, P.O. Box 808, Livermore, California 94550

J. Seely, C. Brown, and U. Feldman
E. O. Hulbert Center, Naval Research Laboratory, Washington, D.C. 20365-5000

G. Glendinning, P. Young, E. Hsieh, and M. Hennesian
Lawrence Livermore National Laboratory, P.O. Box 808, Livermore, California 94550

L. DaSilva
Department of Physics, University of California, Berkeley, Berkeley, California 94720

B. J. MacGowan and D. S. Montgomery
Lawrence Livermore National Laboratory, P.O. Box 808, Livermore, California 94550

C. A. Back
Laboratoire de Physique des Milieux Ionisés, Ecole Polytechnique, 91128 Palaiseau, France

R. Doyas
Lawrence Livermore National Laboratory, P.O. Box 808, Livermore, California 94550

J. Edwards
Blackett Laboratory, Imperial College, London SW7-2BZ, United Kingdom

R. W. Lee
Lawrence Livermore National Laboratory, P.O. Box 808, Livermore, California 94550
(Received 4 May 1992)

The results from a series of experiments that characterize the x-ray flux transmitted through a laser-irradiated Au foil are presented. The purpose of the experiments was to develop a working model for an x-ray source that will create hot, dense plasmas with controllable gradients. These plasmas will be used as a test bed for the study of the complex radiative processes that are intrinsic to the evolution of moderate- and high-Z matter. The experiments quantitatively measured the time- and frequency-dependent energy transferred to the back of the foil. Angular information and the characterization of the flux as a function of foil thickness are also presented. Tables of the time-dependent flux are given.

PACS number(s): 52.25.Nr, 52.50.Jm

I. INTRODUCTION

A. General

The study of plasmas has, over the course of the past 40 years, been motivated and directed by the search for a sustainable fusion plasma [1]. With the advent of laser-produced plasmas, a regime of temperatures and densities arose where the matter was both hot, potentially greater than 1 keV, and relatively dense, with densities quite easily reaching 10^{22} cm^{-3} [2]. This development heralded a generation of experiments to investigate the various detailed phases of the laser-matter interaction. During this period, the characterization of the laser-irradiated high-Z disk, or planar, targets received wide attention [3]. The interest in these targets was motivated by two separate avenues of research.

First, the creation of a high-Z plasma using a laser led to the production of a quasicontinuous M-band emission spectrum that was essentially synchronous with the laser pulse [4]. This, in turn, was itself of importance in that the M-band spectra are composed of myriad unresolved transition arrays (UTA) and are spectroscopically rich. Indeed, for high degrees of ionization the spectroscopy of high-Z elements is largely performed on laser-produced plasmas [5]. Further, the qualities of the emission spectra, i.e., the quasicontinuous spectral nature and the controllable duration, have proved extremely useful in the development of absorption sources in the x-ray region [6].

Second, the plasma produced by the interaction of the laser with a high-Z material is of interest in the study of laser-matter coupling. The formation of gradients, coronal heating, and parametric processes are still the subjects of ongoing investigations [7].

Of these studies, a few have been devoted to the x-ray radiation that is transmitted through the back of thin high-Z foils. Investigations were instigated to further understand the energy coupling of the laser to the high-Z

target [8]. In these studies the amount of radiation transmitted through the target provided additional information on the formation of the shock and radiation waves created by the laser energy deposition on the front surface. The studies of the rear side emission have been motivated by the concept of indirect-drive inertial confinement fusion (ICF) [9]. A discussion of other relevant work will be presented.

B. Specific motivations

The motivation for the present work derives from the fact that the study of hot, dense matter is of specific interest to researchers doing applied work in ICF, x-ray laser studies, astrophysics, and material properties. Previous attempts to create hot, dense matter that could be used to study basic properties have met with little success because they were either not reproducible, e.g., plasma focus machines or vacuum sparks, turbulent and irreproducible, e.g., fast-Z pinches and exploding wires, or produced unresolvable gradients in time and space, e.g., directly irradiated laser-produced plasmas of all kinds. The generation of an x-ray source that can be made reproducible, and can be made intense enough to create matter at temperature from 10 to 100 eV over volumes that are large enough to measure, would be a milestone in the effort to create a laboratory environment which allows access to the physical aspects of hot, dense matter. The ideal source would, of course, behave as a laser in that one would prefer to control the x-ray deposition, the duration of the x-ray source and thus separate the problems of creating the heating source from the study of the matter heated. Using a laser directly is untenable, since the energy deposition will occur at the critical density of material, which for 1-μm laser light is at an electron density N_e of 10^{21} cm^{-3}. This indicates that deposition will not occur in the solid density matter. Thus the laser-solid matter interactions create steep gradients and the hydrodynamics of the heating processes has become a field of study in itself.

We show that a laser can be used to create an x-ray flux which has enough energy to heat a substantial amount of material to tens of electron volts. In addition, we will show that the time scale for the production of the x-ray flux is on the order of the pulse length of the incident laser pulse and therefore we can obtain a heated sample before hydrodynamic expansion causes the sample density to decrease substantially.

C. Layout

The paper is set out in the following way. In Sec. II we discuss the laser used in the experiment. As characterization of the laser beam is essential to ensure that the x-ray flux produced is uniform, a brief description is presented of the Nova laser. Next we discuss the target. The choice of a high-Z material, Au, is discussed, and the motivation for studying a variation in the thicknesses is presented. In this section, a discussion of the experimental setup is given with an emphasis on the diagnostic complement fielded to characterize the x-ray flux. The complement includes a ten-energy-channel, time-resolved, and absolutely calibrated filtered x-ray diode array (FXRD), laser-beam diagnostics, optical streak cameras, a framing camera for imaging of the x-ray region, spectrometer measurements in the UV and x-ray regions, and photoconductive flat-response detectors (PCD's), to measure angular dependence of the rear side flux.

In Sec. III the results of the experiments are presented. Here each of the diagnostic procedures and the resulting data are presented. The emphasis will be on the ten-channel x-ray diode. The time-resolved flux from the nominal 2500-Å foils and the deviations from that case for the other foil thicknesses used, i.e., 1500, 5000, and 7500 Å, are shown. A discussion is given of the time delay between the different energy channels for the different foil thicknesses. Further, we show the results of the Au M-band contributions at $\sim$2500 eV versus the lower-energy x-ray emission for all the foils used. A simple model explaining the various physical processes occurring for the different foils is also presented. Next, the effort to measure the extent to which the laser burns through the foils is discussed, and we show that there is no burn-through. The isolation of the sample from laser irradiation is a critical factor in the eventual performance of experiments.

Section IV is an evaluation of the x-ray source characterization of the nominal 2500-Å foil. We present studies of the uniformity of the x-ray source and the uniformity of the x-ray heating of a test sample where a radiatively heated sample will be located. The angular dependence of the flux is presented from two separate measurements, the FXRD and the PCD. The summary of the data is presented, and in an appendix the time-dependent x-ray flux is presented in tabular form.

II. EXPERIMENTAL SETUP

A. Diagnostic overview

The configuration of this experiment to quantify the x-ray flux was constrained by the geometry of the x-ray heating experiments, which are planned to be performed in the future, where the x-ray flux will be used to provide the sample heating. To illustrate the geometry, a schematic of the x-ray heating experiments is given in Fig. 1(a). The target chamber geometry dictates that the laser propagation direction will be at an angle of 45° or more from the normal of the sample to be heated. The orientation of the target should provide a line of sight, determined by a path from the spectrometer, through the sample to the backlight, that is roughly parallel to the surface of the high-Z foil providing the x-ray flux. These considerations lead to the geometry shown in Fig. 1(b), where the diagnostics used to measure the x-ray flux are shown. The primary diagnostic is a ten-channel filtered x-ray diode system which employs subnanosecond response oscilloscopes to record the signals. This quantifies the x-ray spectrum for one angle in time and energy. To ensure further energy calibration, a set of photoconductive detectors was placed at different angles in the chamber. The isolation of the sample, as shown in Fig. 1(a), from laser light is crucial to ensure the volumetric uniform heating of the sample. To provide in-

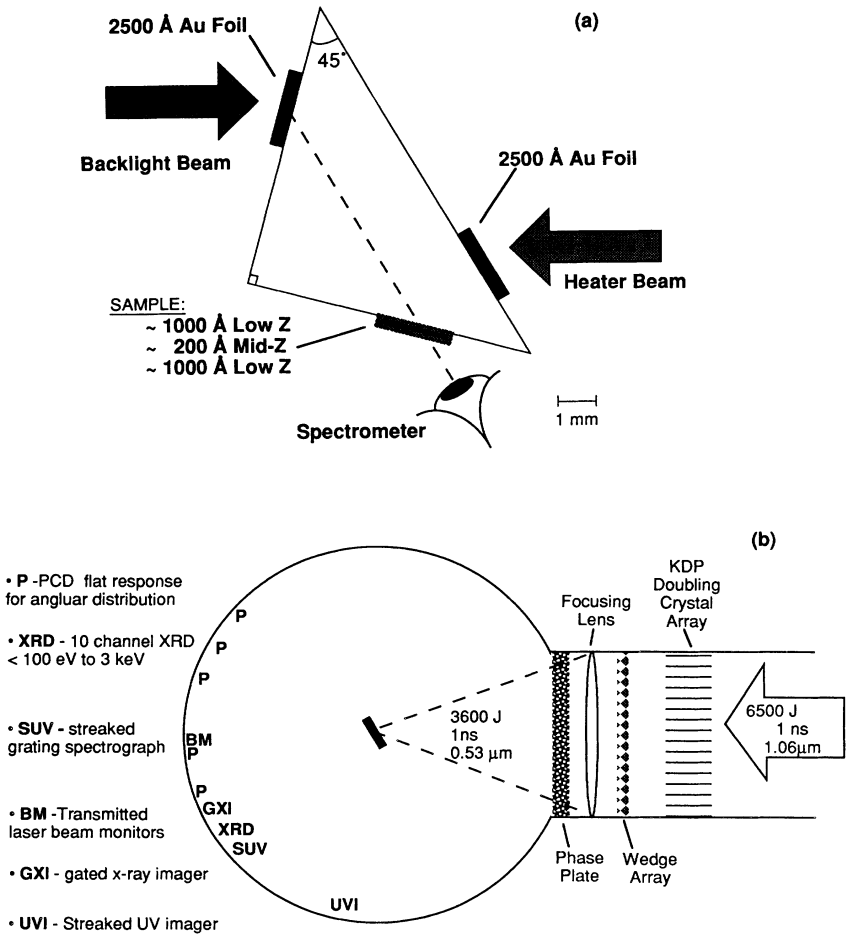

FIG. 1. (a) The schematic of an experimental design to allow quantitative analysis of the absorption spectrum. The key elements in the experiment are the backlight, the sandwiched sample, and a recording medium that allows the various sources to be measured at one time. (b) The experimental setup to measure the x-ray flux emitted from the rear side of a laser-irradiated gold foil. The position of the various diagnostics used in the experimental series is indicated.

formation on laser light burning through the Au foils, transmitted laser-beam diagnostics were employed. Further tests were performed with a streak camera coupled to a UV imaging system which viewed the rear of the Au foil. This provided information on the UV characteristics of the back of the Au foils, that is, the side that is viewed by the sample. Since the uniformity of the heating source is critical to the uniformity of the sample heating—which, in turn, affects the uniformity of the spectroscopic measurements—the UV imager provides information on the heating source and provides corroborating information on the laser burn-through.

A critical aspect of the experimental design is the reproducibility of the laser performance. Since it is well documented that high-intensity high-power lasers give rise to large variations of laser intensity on target with a consequently large variation of x-ray intensity, a monitor of the spatial dependence of the x-ray flux was used [10]. The information determined from these diagnostics indicates that a uniform large-area x-ray source can be produced. The source has been quantified in angle, spectral energy, and time for a series of Au foils.

B. Laser system parameters

The Nova laser was used in the two-beam target chamber. The laser produces approximately 6500 J in a 1-ns flat-top pulse of 1.06-μm light. In Fig. 2(a) the temporal profile of the laser beam is shown as a function of time. To improve coupling of the laser light to the target and reduce the nonlinear parametric processes, the laser is frequency doubled to 0.53-μm light in a potassium diphosphate (KDP) crystal array. Since this laser beam will have large variations in the spatial profile, a set of wedges and then a set of random phase plates are inserted into the beam path. The final beam is 2650 J of 0.53-μm light falling in a roughly 1000-μm spot that is shown in Fig. 2(b). In Fig. 2(b) the beam pattern is shown for a cross-section perpendicular to the propagation axis. Since this beam has amplitude variation of 10 to 1 or less, it is supposed that the processes of laser-target coupling and front-surface plasma formation will lead to a uniform x-ray source at the rear surface of the Au foil. This supposition is borne out by the measurements presented in Sec. III.

C. Target preparation

The targets for the experiments described here are made of Au foils. The foils were free standing and were mounted on large aluminum washers with an inner diameter opening of 0.2 cm. Note that for free-standing Au foils with thicknesses ≤ 500 Å, or for Au foils with

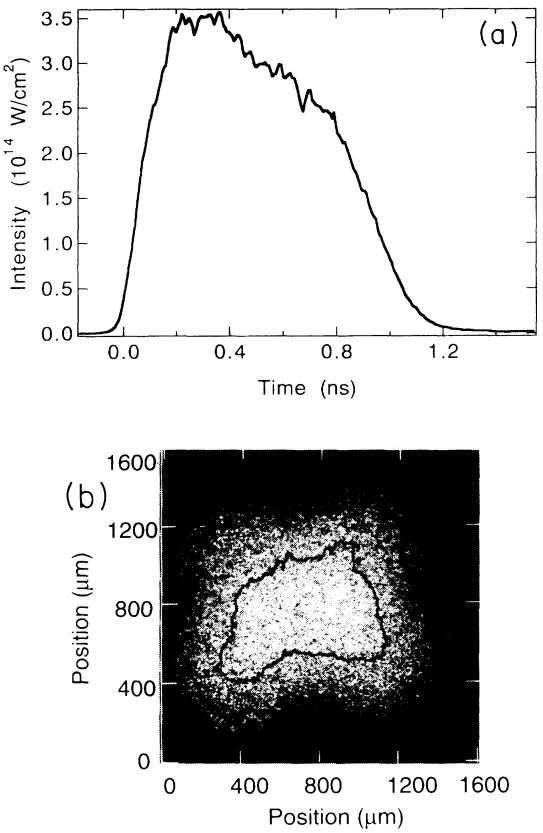

FIG. 2. (a) The Nova laser-beam temporal profile. The beam energy is shown in J/s vs the time in ns. (b) A two-dimensional image of the beam showing the intensity variation of the beam after the process of passing the beam through wedges and random phase plates. Both dimensions are measured in μm and a contour showing the region that is within 10% of the maximum, i.e., the 90% contour is indicated by the thick line.

thicknesses ≤ 1000 Å coated onto CH substrates, pinholes on the order of 10 μm start to appear. The thicknesses chosen for the experiments were 1500, 2500, 5000, and 7500 Å. Thus, the foil thicknesses were chosen to ensure that there were no pinholes in the thinnest targets and that there was substantial x-ray flux from the thickest targets. These measurements serve to quantify a flux that will substantially x-ray heat a sample while maintaining certainty of isolation from laser light and hydrodynamic effects due to the Au foil. The orientation of the target in the chamber was such that the laser-beam axis formed an angle of 30° with respect to the Au foil normal. The accuracy of the target positioning is well below the variation of any of the physical observables, e.g., the intensity, with orientation.

D. Transmitted laser energy

The transmitted laser energy from these Au foil experiments was monitored using an optical streak camera and calorimeter. The laser light that is transmitted through the Au foils passes through a 74-cm aperture $f/4$ lens and impinged on an uncoated, wedged beam splitter. The transmitted laser light reflected by the beam splitter is then relayed to an optical diagnostics area where it is monitored by an optical streak camera. The transmitted light that passes through the beam splitter is monitored by an absorbing-glass calorimeter. There were no detectable signals above background for any of the targets on either the calorimeter or the streak camera, giving an inferred transmitted laser energy of less than 0.1 J total. To confirm the diagnostic, experiments using CH and titanium foils, where one expects the plasma to become transparent during the laser pulse, were used. Indeed, as expected, signals for the transmitted laser energy were measured in the >100-J range for the CH and titanium targets. Therefore, a conservative upper bound on the intensity of 0.53-μm light that could pass through the Au foils is 10^9 W/cm^2, which is below the threshold to substantially affect a sample. This confirms the isolation of the sample region from laser light.

E. UV imaging

The rear surface of the Au foils and the rear side of the sample placed as shown in Fig. 1(a) are imaged with an $f/6$ lens onto an optical streak camera. The system magnification is 10, and this gives a spatial resolution on the order of 25 μm. Filters, made out of BG-12, were placed in front of the streak camera to eliminate light of λ above 0.42 μm. These filters have an attenuation of 10^{-18} at the laser wavelength of 0.53 μm. An optical fiducial synchronized to the laser pulse was inserted onto the imager and was used to determine the timing of the streak camera signal relative to the laser beam. The experimental uncertainty of the timing fiducial and the streak camera is 100 ps. The data from the UV imager was used to ascertain the uniformity of the sample and of the Au foil heating as well as the time-dependent behavior of the x-ray heating.

F. X-ray imaging

The primary diagnostic for the x-ray imaging was a gated pinhole camera. This was an array of four strips, each 6 mm wide of fast-gated microchannel plate (MCP) detectors [11] on a single 40-mm-diam microchannel plate. The burn-through side of the foil was imaged by an array of pinholes onto the four strips, thus providing multiple images at different times with 100-ps time resolution. The time between activation of the strips was typically 300 ps, while the time between frames on a single strip due to pulse transit was 76 ps. The filtering for this camera setup was 0.1 μm of Al on a 0.25-μm CH plastic substrate. The CH was used to filter out the visible and lower-energy UV light. This filtering arrangement transmitted $>80\%$ of the incident x rays with energies above 700 eV. The pinhole was at an angle of 45° above the horizontal and at an azimuthal angle of 60° with respect to the target normal. The combined x-ray imaging system provided a spatial resolution of 10 μm on the target.

G. Photoconductive detectors

The x-ray angular distributions were measured with four diamond photoconductive detectors placed at different angular positions around the target chamber [12]. These detectors were chosen for their flat response to x rays and insensitivity to scattered laser light. They are small devices, 1×1 mm^2 in the active area, which measured the total x-ray energy radiated in the direction defined by the position of the detector at approximately 1 m from the target chamber center. The target could be placed in two orientations with respect to the laser axis. The first orientation had the target plane perpendicular to the ground and tilted 30° from the laser axis towards the XRD, as indicated in Fig. 1(b), giving a 10° angle between the normal of the XRD and the target normal. The other orientation was with the target normal tilted 30° to the other side of the laser axis so that the angle between the XRD normal and the target normal was 70°. This allowed the PCD's to be placed with views of the target from 2°, 22°, 42°, 62°, and 72° from the rear of the Au foil target normal. One detector was placed so that its angle of view did not depend on the rotation of the target. This permitted cross-referencing of experiments performed with targets rotated in the two orientations. The x-ray angular distributions are assumed to be symmetric about the target normal. The detectors as a set were calibrated using the x rays produced from the front surface of a laser-produced plasma with the detectors positioned together in angle and distance from the source.

H. Filtered x-ray diode

The primary instrument for the quantification of the time, angle, and spectral energy-dependent flux is the time-dependent filtered x-ray diode systems. The absolute measurement of the x-ray spectra from ~80 to 1500 eV is achieved by K- and L-edge-filtered x-ray diodes by using an appropriate choice of filter type, thickness, and cathode material [13]. This combination defines a high-sensitivity region just below the absorption edge of the filter that is typically 100–200 eV wide. Although this is a straightforward technique, high-energy sensitivity at photon energies approximately three times that of the primary narrow band contributes to the response. To eliminate this problem, two techniques are employed. First, for channels with primary sensitivity below 600 eV, a grazing-incidence x-ray mirror is used to provide discrimination against high energy. Second, and importantly, one channel is dedicated to the measurement of the high-energy portion of the spectrum. Thus, by judicial choice of the high-energy channel, we can quantitatively correct those channels with high-energy residual contributions. Furthermore, we can determine the contribution to the total energy in the high-energy part of the spectrum, that is, that part of the spectrum above 2000 eV. Since we are interested in the use of the measured x-ray flux as a volume heating source, these x rays can, for thicker samples, play an important role.

The channels used in the current experiments were centered at 70, 100, 275, 425, 500, 675, 825, 1000, 1100, and 2000 eV. The actual responses of the detectors are shown in Fig. 3, as normalized response versus energy in keV. The lower-energy channels have been introduced for this experimental series to help determine the low-energy end of the x-ray flux. All the channels have been absolutely calibrated. The response of the diodes is recorded on fast Tektronix 7250 oscilloscopes with one channel per oscilloscope. The time response of the system is ~100 ps which is deconvolved using a fast Fourier-transform technique while the interchannel temporal accuracy is better than 100 ps. The gross temporal accuracy of the system is therefore better than 150 ps measured with respect to the timing fiducial that is synchronized with the laser pulse.

The method of analyzing the array of ten signals requires a nonlinear fitting procedure, since the response functions of the various channels are energy dependent and since the high-energy contribution must be accounted for self-consistently. In bare outline, initially a spectrum, usually a Planckian, is employed to calculate the expected signal for each channel. The spectrum is then modified by the ratio of measured to calculated signals in the appropriate energy regions. The results of fitting this modification with a smoothing spline is then used as the starting point for the next iteration. Thus, at each iteration a new spectrum, which has been constrained to yield the observed broadband signals, is generated. This process is continued to convergence, typically when agreement between the measured signal and the smooth curve is within ±5%.

In a further effort to ensure that the FXRD provided accurate absolute spectral information, a streak camera coupled to a variable-line-spaced, flat-field grating was set up to resolve the soft x-ray region between 40 and 120 eV [14]. This instrument, together with the use of a time-integrating, spatially resolving grazing incidence spectrometer [15], was used to confirm that the spectrum did indeed behave as the FXRD analysis indicated. These data, together with the fact that the Au spectrum from a laser-produced plasma in the subkilovolt region is com-

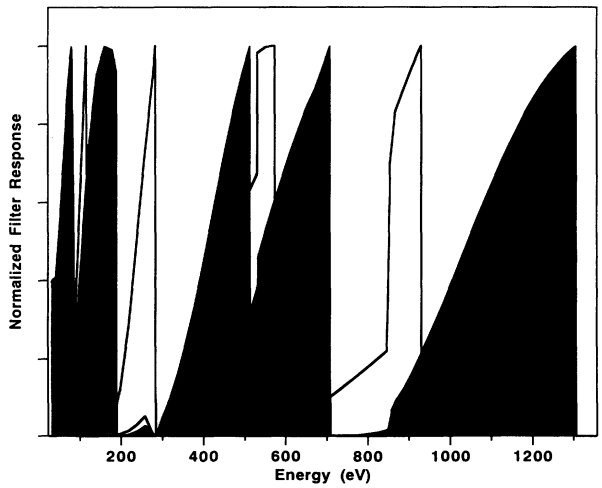

FIG. 3. The response curves for the FXRD channels used in the experimental series. The responses are normalized to a peak of unity for each channel. The energy scale is in eV.

posed of contributions from the N and O bands centered at 800 and 300 eV, respectively, lead to the conclusion that the spectral information from the FXRD is an accurate representation of the flux which is emitted from the rear side of the Au foils.

The placement of the FXRD is fixed in the two-beam target chamber at 135° in θ and 27° in ϕ, with the laser propagation axis being in the positive z direction. This allows testing of the angular dependence of the flux by performing experiments with the target in the two positions of ±30° from the laser axis. Therefore, an energy-dependent measure of the angular dependence at these two angles is obtained.

III. X-RAY CHARACTERIZATION OF Au FOILS OF VARIOUS THICKNESSES

The characterization of the various thickness of Au foils was undertaken to determine the x-ray flux emitted from the back side, i.e., the side not irradiated by the laser beam, and provides a quantitative base for further x-ray heating experiments. The determination of a consistent pattern of behavior of the various physical properties of the x-ray flux with respect to thickness is essential to the understanding of the heating flux.

In Fig. 4 the total energy radiated from the rear side in the low- and high-energy regions is shown as a function of Au foil thickness. The low-energy region includes data from all FXRD channels up to 1500 eV, while the high-energy regions measure the contributions to the spectrum from the Au M bands, i.e., from 2000 to 4000 eV. In Fig. 4 the emitted energy decreases with increasing thickness, with a more rapid decline in the low-energy part of the spectrum than the high-energy part. The different behavior of the two energy bands is consistent with the fact that the low-energy, or thermal, part of the spectrum originates from a radiation wave diffusing into the solid material [16]. The thermal part of the spectrum will be attenuated by the cold matter at the rear of the target and will depend on the depth of penetration of the radiation wave. In contrast, the high-energy part of the emitted spectrum is produced predominantly in the laser-deposition region of the target and depends only on the laser parameters and the target thickness. Since the laser does not burn through the target and since the laser parameters for all the experiments were similar, the amount of energy transmitted should vary with the optical depth of the Au foil to the x rays in the 2000–4000-eV band. In fact, the high-energy contributions do indeed scale as $e^{-\tau}$, where τ is the optical depth in that region.

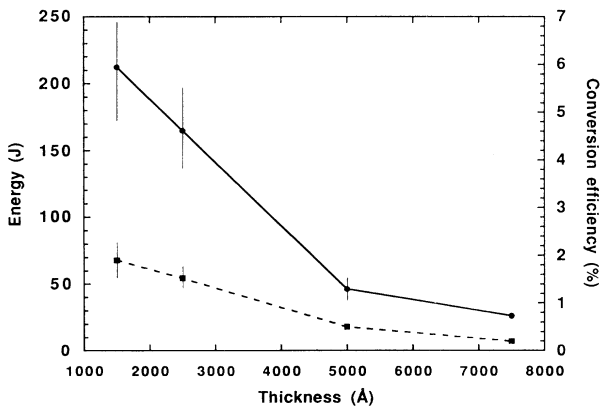

FIG. 4. The variation of the x-ray transmitted energy measured in J on the left-hand ordinate and conversion efficiency, as the percentage of the total transmitted energy divided by the incident $2\omega_0$ laser-beam energy, on the right-hand ordinate vs the target thickness measured in Å. The thermal energy band is shown as a solid line and the M-band channel is represented by a dashed line.

In Fig. 4, the right-hand axis indicates the efficiency of conversion of the laser energy to the energy of the x rays emitted from the rear side. To obtain these conversion efficiencies, the angular distribution of radiation from the rear side is assumed to have a cosine dependence. The data presented in Fig. 8 indicate that the assumption of a $\cos(\theta)$ dependence will not introduce any significant error in the calculation of the conversion efficiency. The conversion efficiency is as high as 8% for the combined thermal and high-energy band contributions for the 1500-Å-thick foil and falls to approximately 1% for the 7500-Å-thick foil. These results can be contrasted to the results contained in the only other comparable measurements made of rear side emission of Au foils by Nishimura *et al.* [17]. In that paper the results for conversion were presented for 0.35-μm light impinging on Au foils. Assuming approximately 85% absorption, an indirect comparison can be made between the present case of 5000-Å-thick Au foil and the Nishimura *et al.* case of 5600-Å-thick Au foil. Nishimura *et al.* report peak intensities of 550 J/keV ns into 4π, which compares to the peak intensities of approximately 600 J/keV ns into 4π in the present study. This should be considered fortuitously good agreement, since the Nishimura experiments had large-amplitude laser-beam modulations and were subject to lateral energy transport due to the rather small spots used. These effects will not be a problem in the present experiment, since the beam has been smoothed, and measurements have been made to ensure that hot spots do not affect the data, and the spots are very large.

To compare the temporal behavior of the different thickness foils, the evolution of a single energy band is analyzed. In Fig. 5 the intensity of the emission at 300 eV measured in J/keV ns into 4π is plotted against time in ns. The 300-eV part of the spectrum represents the peak of the thermal part of the emission. First, note that there is a steady decrease in the intensity with increasing thickness, consistent with the total energy emitted. Second, with increasing thickness there is an increase in the time delay before the thermal part of the spectrum rises to a peak. This time delay is consistent with the formation of a radiation wave which penetrates the Au foil. For the thinner foils, the radiation wave creates a thermal hot, dense plasma which is only slightly attenuated by the remaining cold plasma, while in the thicker foils the radiation wave must penetrate the foil for a longer time before the radiation can escape effectively. The time delay to the peak of the emission can be noted

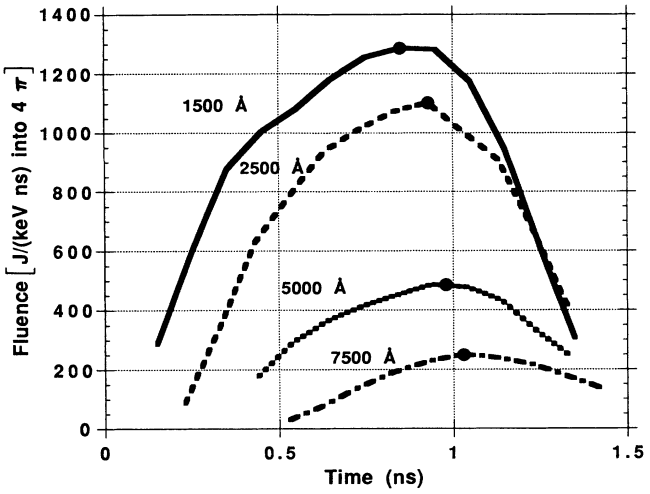

FIG. 5. The time history of the 300-eV channel for various different target thicknesses. The time is measured in ns with the time zero (0.00) measured from the laser pulse initiation. The fluence is measured in J/keV ns radiated into 4π. The peak of the different curves is indicated by a closed circle so that the successively lengthening time delay with increasing target thickness can be observed.

by the symbol ● placed on the peak of the emission. This represents, in part, the radiation diffusion velocity. The results in Fig. 5 are in distinction to the time dependence of the high-energy part of the transmitted spectrum. The results for the high-energy contributions show no discernible time delay relative to each other. The peak of the high-energy band contribution comes at 0.88 ns, which matches the peak of the 1500-Å-foil thermal transmission peak.

The relative behavior of the total energy and time dependence for foils of different thicknesses has been measured. The 2500-Å-thick Au target is chosen for detailed examination based on the observation that it does not burn through and provides more than 200 J of energy in an x-ray pulse lasting 1 ns. This is a conservative choice to ensure isolation and sufficient heating to produce a hot, dense plasma.

IV. THE EXPERIMENTAL CONFIGURATION: THE 2500-Å Au FOIL

The results for the response of the different foil thicknesses are presented in Sec. III; in the present section we present a more detailed study of the results for the 2500-Å foil. These results, together with those of Sec. III, provide an understanding of the transmitted x-ray flux from the Au foils.

A. Time-dependent x-ray fluence

The time-dependent measurement of the x-ray fluence transmitted through the Au foil of 2500 Å is shown in Figs. 6(a) and 6(b) as J/keV ns radiated into a sphere. The abscissa is measured in keV and only the thermal contribution is shown. The M-band contributions at energies greater than 2 keV are represented in a single

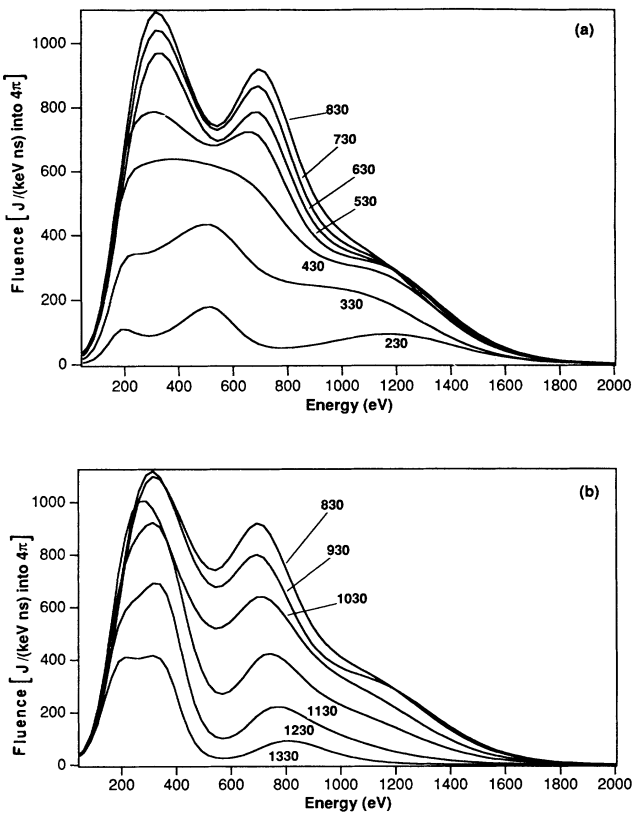

FIG. 6. The x-ray fluence in J/keV ns radiated into 4π from the rear side of the 2500-Å Au foil vs spectral energy in keV for various times. (a) Early times from 0.23 ns after laser pulse initiation to 0.83 ns, and (b) late times from 0.83 to 1.33 ns.

channel and are presented in the Appendix in tabular form. The label on each of the curves represents times measured from the initiation of the laser pulse.

The initial-time data are relatively flat with little discernible structure. As the laser pulse creates a radiation wave in the solid Au, the formation of a dominant Au N- and O-band structure is observed. The N band of Au, at $\sim$750 eV, and the O band, at $\sim$275 eV, dominate the spectrum. The peak of the spectrum is seen to occur near the end of the 1-ns laser pulse at 0.83 ns and the decrease in the transmitted energy occurs most rapidly to the highest-energy components of the spectrum. Thus, the N band decays first and the final spectrum shown in Fig. 6(b) has a dominant O-band contribution. That the highest-energy contribution decays fastest after the laser pulse has ended is consistent with the view that the M band is produced predominantly in the front side laser-matter interaction region, while the thermal contributions come from the radiation wave diffusing into the solid. Thus, the N-band contributions would arise from a combination of emission from the two regions.

As a representation of the total transmitted energy, the rear surface of the Au foil could be characterized as an equivalent blackbody emitter by equating the integrated spectral energy output to that emitted from a blackbody for the measured emission area. This blackbody representation of the radiation emitted from these high-Z irra-

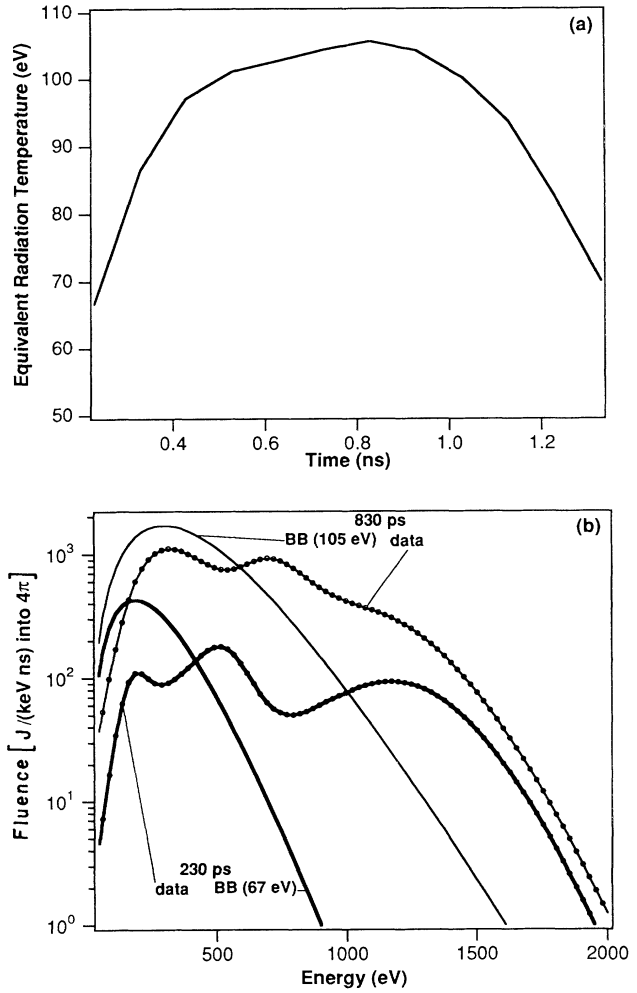

FIG. 7. (a) The time history of the total energy emitted from the back side of the 2500-Å Au foil as an equivalent blackbody temperature vs time in ns. (b) The spectral energy of the equivalent blackbody (solid curves) compared to the measured spectrum (solid curve with dot) vs energy in eV for the times 0.23 and 0.73 ns.

diated foils is inherent in schematic models used to analyze the physical processes occurring in the conversion of laser light to x rays [8,9,16,17]. Further, the representation of the emitted energy as a blackbody source yields a simple view of the time dependence of the fluence. The results are shown in Fig. 7, where the time-dependent radiation temperature derived from the *thermal* part of the spectrum is shown in Fig. 7(a), while a comparison of the equivalent blackbody versus the true spectral shape is shown in Fig. 7(b) for two times in the evolution of the radiation. The M-band, or high-energy contributions have not been included in the integration, as the M-band flux is assumed to be created by laser-plasma interactions, and not as emission from a radiation front. Inclusion of the M bands should therefore be considered as an additional contribution with a separate parametrization. On the one hand, it is clear from Fig. 7(a) that this simple parametrization of the energy in the radiation field is useful. However, it must be pointed out that the spectral character of the x-ray flux is strongly non-Planckian even for the thermal region, as illustrated in Fig. 7(b). Thus, the utility of the simple representation for the thermal part of the spectrum is limited.

B. Angular distribution of the flux

The angular distribution of the transmitted radiation is important to the uniform heating of a sample that is separated from the Au burn-through foil by a few mm. The uniformity of the sample and the reproducibility of the flux from the rear surface are critical to the predictability of the sample heating. In the experiments, we have measured the angular distribution of the radiation by two methods. First, PCD's have been placed at various angles with respect to the rear surface normal. These detectors will provide extremely accurate integrated flux measurements and provide the primary angular response data. Second, to corroborate the PCD results and provide information on the differences in angular emission of the various different energies, the FXRD is placed at two different angles with respect to the rear surface normal. The placement of the FXRD was chosen to reproduce angles that the PCD's measured.

The results for the angular dependence of the flux are shown in Fig. 8, where the flux normalized to unity at an angle perpendicular to the rear surface is shown versus the angle from the normal. The results show a good fit to a cosine law distribution. The results of the comparison for the FXRD and the PCD show that the two measurements are in agreement for the angles near 0° and 70°. The energy dependence of the angular emission is extracted from the FXRD data and can be summarized as follows: The bulk of the distribution of energy, that is, those channels above 100 eV, does not show any variation from the angular results for the integrated spectrum. However, there is some indication that the lowest-energy channels do have a more rapid decrease with increasing

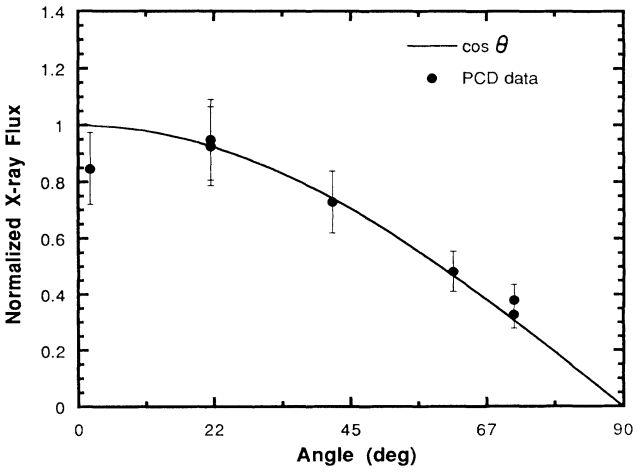

FIG. 8. The integrated flux normalized to unity at 0° vs the angle of observation measured from the rear surface normal of the 2500-Å Au burn-through foils. The cos(θ) distribution is shown for comparison as a solid line.

angle than the higher-energy channels. This is expected, since the low-energy radiation has a relatively larger optical depth than the high-energy radiation. Thus, the energy channels lower than 100 eV have a decidedly non-Lambertian character when one views the back surface as the radiator. The integrated energy content is insensitive to these low-energy channels, since the bulk of the radiation arises from the spectral regions above 100 eV.

C. Spatial images—UV and x ray

The direct measurement of the spatial uniformity of the rear surface emission is also measured. The occurrence of hot spots due to laser deposition on the front surface or macroscopic fluctuations in the laser which would induce nonuniformities in the rear surface emission are unacceptable factors in the generation of an x-ray radiation [17]. We have measured the rear-side transmitted flux at low energies using a streak camera coupled to an UV filtered imaging slit having a response in a spectral band ~ 3 eV and in the x-ray region responding to a band above 800 eV using a multiframe gated x-ray imaging device. The low-energy emission indicates the level of uniformity of the low-energy band and provides information on any laser-induced patterns that will be transmitted to the rear surface. Further, the UV imaging arrangement allowed us to measure the uniformity of the heating of the sample, which is positioned approximately 2 mm from the Au burn-through foil. The x-ray gated images give us information on the bulk of the energy transported to the rear. Since the smoothing of the beam is achieved with wedges and phase plates, the beam pattern on the angled target is shaped like a slightly deformed "four-leafed clover."

In Fig. 9 the two-dimensional pattern of the rear-side x-ray flux is shown. As can be seen by the scale, the spot is uniform over approximately 1 mm, and the intensity pattern over the central portion of the image is shown in Fig. 9. This shows the size and uniformity of the x-ray spot. The time history of the x-ray flux was measured on the multiple frames of the imager, and it is found that the radiation in this band does not change size during the laser pulse.

In Fig. 10 the streak camera record of the rear side of the Au foil is shown with time in ns, increasing in the vertical and distance along the target on the horizontal. Note that the edges of the spot slightly widen as time increases, indicating a spreading of the spot in the lateral direction during the laser pulse. The relative timing of the streak camera to the laser pulse is provided by the insertion of a fiducial timing mark generated in the primary stages of the laser pulse generation and provides a timing accuracy of 30 ps. In Fig. 11(a) the horizontal uniformity of the spot is shown to be good, with the main spot covering > 1 mm.

D. Uniformity of sample heating

The goal of the development of this x-ray source is to provide uniform heating of a hydrodynamically isolated sample which will not have critical density surface in-

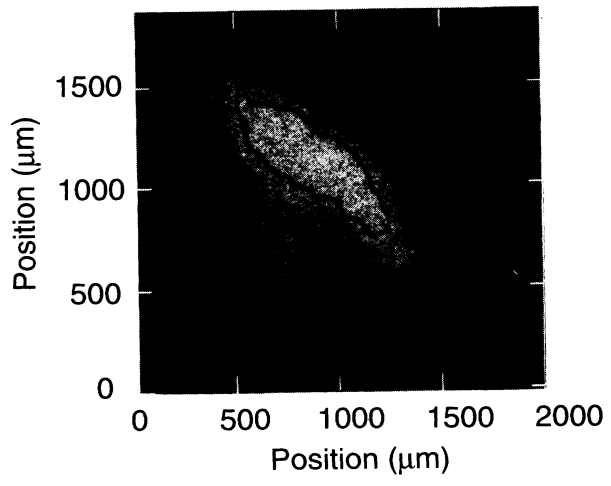

FIG. 9. The two-dimensional image of the rear side of the 2500-Å Au burn-through foil filtered to show the intensity of the energy band from 800 eV. The ordinate and the abscissa are measured in μm and this image is taken at 0.07 ns. As an indication of the intensity uniformity, the region of the x-ray foil that is within 10% of the maximum, i.e., the 90% contour, is shown on the image by the thick line.

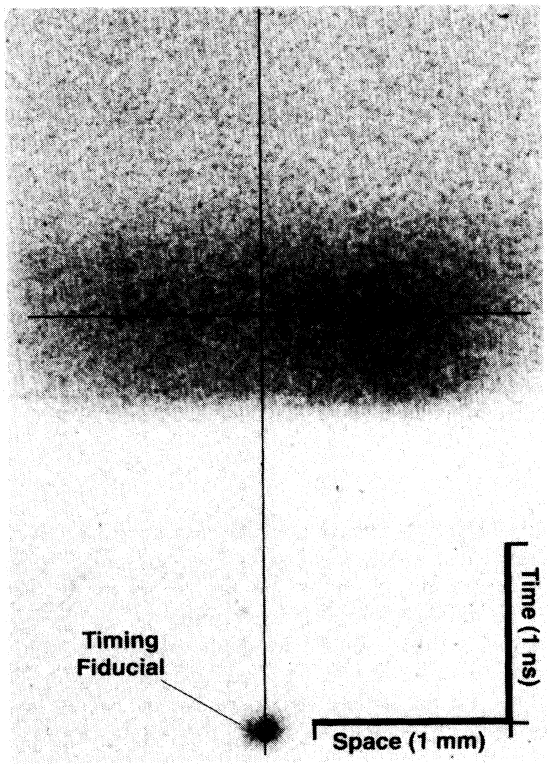

FIG. 10. The UV imaging streak camera record measuring the UV energy band around 3.1 eV. The spatial dimension is horizontal and the time axis is vertical. Note that the width of the transmitting region grows slightly in time. The vertical and horizontal lines indicate the positions where the curves presented in Fig. 11 are taken. The scale of the time and length axes is indicated by the bar in the lower right.

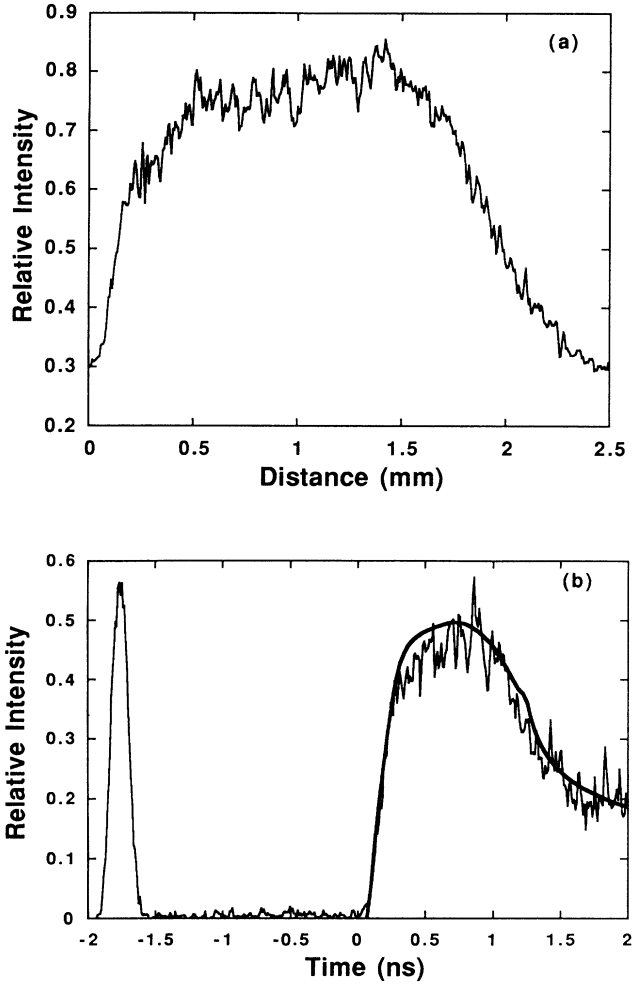

FIG. 11. Data along the lines indicated in Fig. 10. (a) The relative intensity of the rear side at a time 0.2 ns measured along the target. (b) The relative intensity of the transmission of the UV signal through the 2500-Å foil as a function of time measured in ns relative to the initiation of the laser pulse. Note that the data represented as a thin line include the timing fiducial. The thick line is a simulation of the UV transmission using the measured x-ray flux as data.

teractions or hydrodynamic interference in its evolution. The final test of the x-ray source is, therefore, to heat an aluminum foil placed in the sample position shown in Fig. 1(a) and measure the uniformity of the heating. To accomplish this, the UV imaging diagnostic was implemented to observe the rear side of the *sample*. In this way we can determine two parameters: first, the spatial uniformity of the heating due to the radiation source, and second, the evolution of the heated sample given the measured time-dependent x-ray flux.

To ascertain the time evolution of the UV emission from the rear side of a 2500-Å Au foil, we use the measured x-ray flux as input to a hydrodynamics simulation [7]. Since the flux was measured for energies >80 eV, the simulation, with the experimentally determined x-ray source as input, is required to generate the UV emission history by placing the source in a thin Au layer. This procedure allows one to indirectly verify the extrapolation of the experimental data to low energies, while permitting the transmitted x rays to heat a sample in the simulation. In Fig. 11(b) we compare the measured intensity as a function of time—a horizontal sample from Fig. 10—with the simulation. Here the fiducial marker is shown along with the experimentally determined emission. The results show good agreement for the onset and the intensity shape. The method chosen to introduce the measured x-ray flux into the simulation was to place the time-dependent x-ray flux in a thin Au layer. In this way the very-low- and very-high-energy regions each play a role in the x-ray flux, even though the measurements, using the filtered x-ray diodes, did not measure these spectral regions. Thus, the result in Fig. 11 corroborates that the bulk of the data used is accurate. At late time, >1 ns, the observed rapid dropoff of the emission correlates with the laser pulse decay. The simulation of the Au layer serves as an energy source and the slight discrepancy at late times is an artifact of not including the hydrodynamics expansion, which would dissipate the energy.

The measurement of the emission of a 2-μm-thick aluminum foil heated by x rays transmitted from the rear of the nominal 2500-Å Au foil is shown in Fig. 12. Here the streak camera record shows the time history of the Al foil in emission. The uniformity along the horizontal dimension can be seen in Fig. 13(a), where the relative intensity is shown as a function distance measured in mm along the Al foil. Note that the entire plate is imaged and that in the proposed experiments only a fraction of the total horizontal distance will be used and is indicated by shading. Note that a simple viewing-angle calculation of the flux on the target, which takes into account the distance and angle between the burn-through foil and the sample, is shown in Fig. 13(a) as a dotted line. The uni-

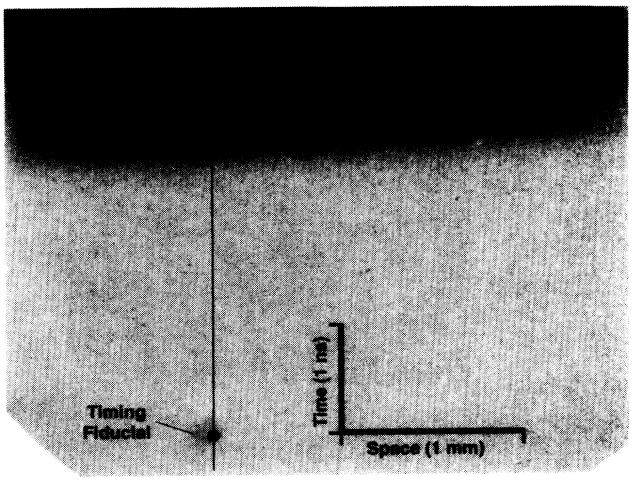

FIG. 12. The streaked UV image record with time in ns and space along an aluminum sample, placed as indicated in Fig. 1(a). The vertical and horizontal lines indicate the positions where the curves presented in Fig. 13 are taken. The scale of the time and length axes is indicated by the bar in the lower right.

formity of the heated sample is therefore measured to be better than ±5% and is in good agreement with the view factor calculation.

The time evolution of the UV emission from the Al foil was also simulated using the same x-ray source that produced the UV calculation in Fig. 11. The results for the Al emission are shown in Fig. 13(b), where the relative intensity is presented as a function of time in ns for a vertical line running through the fiducial marker in Fig. 12. The results for the experiment show that the Al plate heats up slowly, peaks, and then decays slowly. The simulation does precisely the same but with a slight variation in the rise time of the pulse. These results are considered encouraging, since the uniformity and the overall time histories are predictable and therefore amenable to calculation.

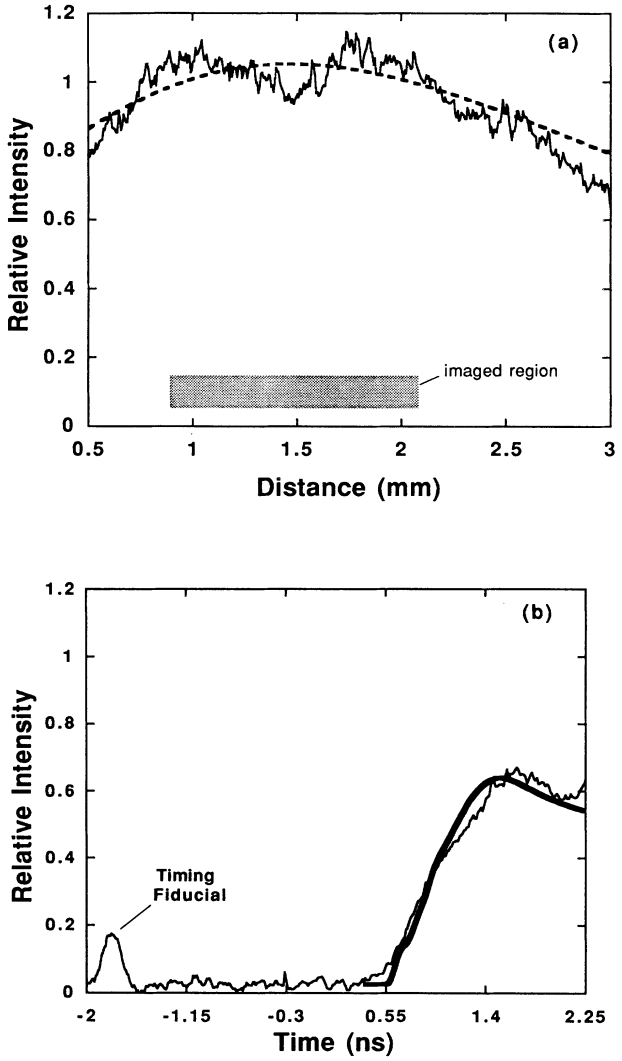

FIG. 13. Data along the lines indicated in Fig. 12. (a) The uniformity of the sample heating of the aluminum foil taken as the relative intensity of a horizontal line at time 0.2 ns vs the distance in mm along the target. The shaded region indicates the region of the sample that would be imaged in a full experimental configuration. The dotted line is a simple view factor calculation of the relative intensity across the sample given the known flux and the geometry. (b) The evolution of sample heating measured by taking a vertical line through the fiducial marker. The time is measured in ns and the ordinate is relative intensity. The thin line represents the data including the fiducial, while the thick line represents the simulation of the rear side emission of the aluminum plate.

V. DISCUSSION

The emission from the rear surface has previously been studied as a method of ascertaining the details of the radiation wave that forms behind the critical density surface in the solid material [17,8]. In these previous reports, small laser spot sizes and laser-beam hot spots have given rise to uncertainty in the measurement of the x-ray flux. In fact, the imaging used in Ref. [17] shows the hot spots due to the intensity variation of the incident laser beam on the *back* of the target. The results presented here show that beam smoothing is effective in controlling the x-ray uniformity of the rear surface. Further, the difficulty presented by beam nonuniformity, i.e., the laser burning through to the rear surface, has been effectively removed. The assurance that direct laser irradiation of the sample does not occur is essential to the design of a pure x-ray flux environment.

The points of comparison with Ref. [17] are (i) the rear side conversion efficiency and (ii) the time dependence of the various spectral bands for similar thickness targets. First, in the case of the conversion efficiency, we find that for the 5000-Å foil, our conversion efficiency is a factor of 3 smaller. This difference is most likely due to the existence of hot spots in the laser beam, reported for the experiments in Ref. [17], which will give rise to a more rapid penetration of the Au foil, either by higher intensity laser spots or by secondary processes such as hot electrons. The differences in wavelength and the slight difference in foil thickness between the present experiment and those reported in Ref. [17] cannot lead to this discrepancy. On the one hand, the wavelength of the laser would be important only if the absorption fraction were different for the two wavelengths; however, the absorption for both 2ω and 3ω light at angles less than 45° from the normal is approximately the same. Thus, given the same absorption fraction, the difference would have to be attributable to the differences due to the distinct critical densities in the two experiments. On the other hand, the slight differences in the foil thicknesses in the two experiments cannot give rise to the discrepancy, since the 12% difference in thickness would only serve to increase, not decrease, the discrepancy. Note that the trend of the conversion efficiency versus foil thickness shown in Fig. 4 is unambiguous and indicates that a 12% conversion is inconsistent with the results shown in, and the comments made concerning, Fig. 9 of Ref. [17].

Second, the present measurement that can be compared with those of Ref. [17] is the time history of the *O* and *N* spectral bands emitted from the rear surface. Comparing the 0.436-μm-thick foil in Ref. [17] to the 5000-Å foil, we find that in the data the rise of the *O* and *N* bands occurs simultaneously, within the accuracy of the instrument, i.e., ~100 ps. The decay time of the

TABLE I. The time-dependent x-ray source measured from the rear of a 1500-Å Au foil. The units for the thermal part of the distribution, specified at energies in keV from 0.1 to 1.8, are J/keV ns into 4π. The units for the M band specified as M are J/ns into 4π. The times are in ns from 0.15 to 1.25. The notation used (1.55[+1]) represents 1.55×10^{1}.

Energy (keV) \ Time (ns)	0.15	0.25	0.35	0.45	0.55	0.65	0.75	0.85	0.95	1.05	1.15	1.25
0.1	1.78[+1]	5.97[+1]	9.91[+1]	1.17[+2]	1.23[+2]	1.31[+2]	1.41[+2]	1.45[+2]	1.45[+2]	1.41[+2]	1.32[+2]	1.17[+2]
0.2	8.42[+1]	3.31[+2]	5.54[+2]	6.59[+2]	6.90[+2]	7.42[+2]	7.93[+2]	8.16[+2]	8.11[+2]	7.52[+2]	6.43[+2]	4.81[+2]
0.3	2.88[+2]	5.92[+2]	8.75[+2]	1.00[+3]	1.08[+3]	1.18[+3]	1.25[+3]	1.28[+3]	1.28[+3]	1.18[+3]	9.50[+2]	6.15[+2]
0.4	1.04[+2]	3.84[+2]	6.87[+2]	8.14[+2]	8.62[+2]	9.18[+2]	9.73[+2]	9.75[+2]	9.72[+2]	9.22[+2]	7.65[+2]	5.03[+2]
0.5	2.35[+1]	2.90[+2]	5.93[+2]	7.56[+2]	7.97[+2]	8.36[+2]	8.80[+2]	8.77[+2]	8.19[+2]	6.98[+2]	4.69[+2]	2.48[+2]
0.6	3.05[+1]	3.23[+2]	6.52[+2]	8.65[+2]	9.59[+2]	1.01[+3]	1.06[+3]	1.06[+3]	9.41[+2]	6.91[+2]	3.62[+2]	1.44[+2]
0.7	8.75[+1]	3.68[+2]	7.16[+2]	9.40[+2]	1.11[+3]	1.17[+3]	1.25[+3]	1.25[+3]	1.11[+3]	7.60[+2]	3.71[+2]	1.32[+2]
0.8	4.06[+1]	2.70[+2]	5.72[+2]	7.35[+2]	8.59[+2]	8.72[+2]	9.68[+2]	9.68[+2]	8.86[+2]	6.48[+2]	3.79[+2]	1.63[+2]
0.9	1.07[+1]	1.77[+2]	4.12[+2]	5.21[+2]	5.80[+2]	5.69[+2]	6.45[+2]	6.44[+2]	6.12[+2]	4.97[+2]	3.58[+2]	1.95[+2]
1.0	8.69[+0]	1.54[+2]	3.44[+2]	4.35[+2]	4.69[+2]	4.62[+2]	5.12[+2]	5.12[+2]	4.93[+2]	4.20[+2]	3.11[+2]	1.71[+2]
1.1	1.71[+1]	1.63[+2]	3.15[+2]	4.02[+2]	4.27[+2]	4.36[+2]	4.58[+2]	4.61[+2]	4.41[+2]	3.74[+2]	2.46[+2]	1.14[+2]
1.2	4.20[+1]	1.70[+2]	2.79[+2]	3.60[+2]	3.80[+2]	4.06[+2]	4.02[+2]	4.06[+2]	3.84[+2]	3.17[+2]	1.77[+2]	6.52[+1]
1.3	7.74[+1]	1.52[+2]	2.16[+2]	2.82[+2]	2.96[+2]	3.29[+2]	3.10[+2]	3.14[+2]	2.93[+2]	2.37[+2]	1.14[+2]	3.48[+1]
1.4	1.01[+2]	1.14[+2]	1.45[+2]	1.92[+2]	2.01[+2]	2.29[+2]	2.08[+2]	2.12[+2]	1.95[+2]	1.55[+2]	6.71[+1]	1.76[+1]
1.5	9.50[+1]	7.26[+1]	8.62[+1]	1.14[+2]	1.19[+2]	1.39[+2]	1.23[+2]	1.25[+2]	1.15[+2]	9.02[+1]	3.61[+1]	8.56[+0]
1.6	6.71[+1]	4.02[+1]	4.55[+1]	6.06[+1]	6.33[+1]	7.46[+1]	6.47[+1]	6.62[+1]	6.05[+1]	4.70[+1]	1.79[+1]	3.98[+0]
1.7	3.65[+1]	1.95[+1]	2.16[+1]	2.89[+1]	3.01[+1]	3.57[+1]	3.08[+1]	3.15[+1]	2.87[+1]	2.22[+1]	8.29[+0]	1.78[+0]
1.8	1.57[+1]	8.45[+0]	9.38[+0]	1.25[+1]	1.31[+1]	1.55[+1]	1.33[+1]	1.37[+1]	1.25[+1]	9.65[+0]	3.59[+0]	7.74[−1]
M	32.0	110.0	185.0	235.0	270.0	300.0	320.0	325.0	310.0	255.0	145.0	45.0

TABLE II. The time-dependent x-ray source measured from the rear of a 2500-Å Au foil. The units for the thermal part of the distribution, specified at energies in keV from 0.1 to 1.8, are J/keV ns into 4π. The units for the M band specified as M are Joules per ns into 4π. The times are in ns from 0.23 to 1.33. The notation used (1.85[+1]) represents 1.85×10^{1}.

Energy (keV) \ Time (ns)	0.23	0.33	0.43	0.53	0.63	0.73	0.83	0.93	1.03	1.13	1.23	1.33
0.1	2.33[+1]	6.77[+1]	1.10[+2]	1.29[+2]	1.11[+2]	1.18[+2]	1.27[+2]	1.35[+2]	1.54[+2]	1.51[+2]	1.37[+2]	1.18[+2]
0.2	1.11[+2]	3.21[+2]	5.40[+2]	6.43[+2]	5.71[+2]	6.23[+2]	6.68[+2]	6.99[+2]	7.89[+2]	7.07[+2]	5.58[+2]	4.05[+2]
0.3	8.88[+1]	3.48[+2]	6.29[+2]	7.86[+2]	9.50[+2]	1.03[+3]	1.09[+3]	1.11[+3]	9.96[+2]	9.17[+2]	6.80[+2]	4.15[+2]
0.4	1.26[+2]	3.96[+2]	6.38[+2]	7.45[+2]	8.94[+2]	9.44[+2]	9.76[+2]	9.55[+2]	7.60[+2]	7.31[+2]	5.22[+2]	2.68[+2]
0.5	1.78[+2]	4.34[+2]	6.24[+2]	6.85[+2]	7.22[+2]	7.54[+2]	7.66[+2]	7.13[+2]	5.48[+2]	3.41[+2]	1.54[+2]	4.67[+1]
0.6	1.25[+2]	3.80[+2]	5.96[+2]	7.04[+2]	7.24[+2]	7.72[+2]	7.93[+2]	7.09[+2]	5.46[+2]	2.84[+2]	1.07[+2]	2.66[+1]
0.7	6.09[+1]	2.93[+2]	5.34[+2]	7.07[+2]	7.83[+2]	8.64[+2]	9.19[+2]	8.00[+2]	6.39[+2]	4.05[+2]	1.90[+2]	6.15[+1]
0.8	4.99[+1]	2.55[+2]	4.29[+2]	5.47[+2]	6.18[+2]	6.83[+2]	7.49[+2]	6.45[+2]	5.60[+2]	3.93[+2]	2.16[+2]	9.10[+1]
0.9	6.00[+1]	2.43[+2]	3.45[+2]	3.97[+2]	4.36[+2]	4.72[+2]	5.24[+2]	4.55[+2]	4.21[+2]	2.93[+2]	1.63[+2]	7.28[+1]
1.0	7.55[+1]	2.32[+2]	3.11[+2]	3.38[+2]	3.59[+2]	3.80[+2]	4.11[+2]	3.70[+2]	3.35[+2]	2.28[+2]	1.14[+2]	3.99[+1]
1.1	8.89[+1]	2.11[+2]	2.93[+2]	3.18[+2]	3.26[+2]	3.36[+2]	3.48[+2]	3.30[+2]	2.76[+2]	1.84[+2]	7.73[+1]	1.74[+1]
1.2	9.21[+1]	1.75[+2]	2.60[+2]	2.87[+2]	2.86[+2]	2.90[+2]	2.84[+2]	2.85[+2]	2.16[+2]	1.41[+2]	4.94[+1]	6.90[+0]
1.3	8.02[+1]	1.28[+2]	2.02[+2]	2.27[+2]	2.20[+2]	2.19[+2]	2.07[+2]	2.16[+2]	1.51[+2]	9.67[+1]	2.92[+1]	2.75[+0]
1.4	5.91[+1]	8.21[+1]	1.36[+2]	1.55[+2]	1.48[+2]	1.45[+2]	1.33[+2]	1.43[+2]	9.45[+1]	5.95[+1]	1.60[+1]	1.12[+0]
1.5	3.73[+1]	4.71[+1]	8.07[+1]	9.27[+1]	8.73[+1]	8.52[+1]	7.60[+1]	8.41[+1]	5.31[+1]	3.31[+1]	8.22[+0]	4.65[−1]
1.6	2.04[+1]	2.43[+1]	4.26[+1]	4.92[+1]	4.60[+1]	4.47[+1]	3.93[+1]	4.41[+1]	2.71[+1]	1.68[+1]	3.97[+0]	1.97[−1]
1.7	9.87[+0]	1.15[+1]	2.03[+1]	2.35[+1]	2.19[+1]	2.12[+1]	1.85[+1]	2.09[+1]	1.27[+1]	7.84[+0]	1.81[+0]	8.45[−2]
1.8	4.26[+0]	4.96[+0]	8.78[+0]	1.02[+1]	9.47[+0]	9.18[+0]	8.02[+0]	9.07[+0]	5.50[+0]	3.40[+0]	7.85[−1]	3.68[−2]
M	60.0	129.0	185.0	215.0	235.0	255.0	270.0	267.0	225.0	145.0	57.0	9.0

TABLE III. The time-dependent x-ray source measured from the rear of a 5000-Å Au foil. The units for the thermal part of the distribution, specified at energies in keV from 0.1 to 1.8, are J/keV ns into 4π. The units for the M band specified as M are J/ns into 4π. The times are in ns from 0.44 to 1.34. The notation used (1.51[−1]) represents 1.55×10^{-1}.

Energy (keV) \ Time (ns)	0.44	0.54	0.64	0.74	0.84	0.94	1.04	1.14	1.24	1.34
0.1	4.27[+1]	6.95[+1]	8.84[+1]	1.00[+2]	1.08[+2]	1.16[+2]	1.22[+2]	1.18[+2]	1.07[+2]	8.93[+1]
0.2	1.94[+2]	3.16[+2]	3.95[+2]	4.43[+2]	4.77[+2]	5.11[+2]	5.13[+2]	4.70[+2]	3.86[+2]	2.96[+2]
0.3	1.76[+2]	2.91[+2]	3.66[+2]	4.16[+2]	4.53[+2]	4.87[+2]	4.82[+2]	4.39[+2]	3.33[+2]	2.41[+2]
0.4	1.35[+2]	2.65[+2]	3.55[+2]	4.15[+2]	4.54[+2]	4.77[+2]	5.01[+2]	4.46[+2]	3.21[+2]	2.00[+2]
0.5	8.01[+1]	1.66[+2]	2.23[+2]	2.69[+2]	3.03[+2]	3.23[+2]	2.89[+2]	1.99[+2]	1.11[+2]	5.74[+1]
0.6	7.76[+1]	1.38[+2]	1.76[+2]	2.07[+2]	2.21[+2]	2.17[+2]	1.55[+2]	7.88[+1]	3.31[+1]	1.14[+1]
0.7	1.05[+2]	1.53[+2]	1.85[+2]	2.03[+2]	1.96[+2]	1.69[+2]	1.08[+2]	4.58[+1]	1.55[+1]	2.55[+0]
0.8	8.57[+1]	1.28[+2]	1.50[+2]	1.61[+2]	1.54[+2]	1.31[+2]	8.77[+1]	3.75[+1]	1.06[+1]	6.41[−1]
0.9	4.73[+1]	8.26[+1]	9.66[+1]	1.05[+2]	1.06[+2]	9.57[+1]	7.29[+1]	3.45[+1]	8.36[+0]	1.79[−1]
1.0	2.38[+1]	4.83[+1]	5.65[+1]	6.20[+1]	6.62[+1]	6.36[+1]	5.48[+1]	2.85[+1]	6.11[+0]	5.51[−2]
1.1	1.15[+1]	2.64[+1]	3.09[+1]	3.43[+1]	3.82[+1]	3.86[+1]	3.66[+1]	2.06[+1]	4.01[+0]	1.86[−2]
1.2	5.39[+0]	1.35[+1]	1.59[+1]	1.78[+1]	2.05[+1]	2.15[+1]	2.19[+1]	1.31[+1]	2.38[+0]	6.85[−3]
1.3	2.44[+0]	6.54[+0]	7.70[+0]	8.69[+0]	1.03[+1]	1.11[+1]	1.19[+1]	7.37[+0]	1.28[+0]	2.73[−3]
1.4	1.07[+0]	2.99[+0]	3.54[+0]	4.02[+0]	4.82[+0]	5.29[+0]	5.85[+0]	3.72[+0]	6.35[−1]	1.17[−3]
1.5	4.60[−1]	1.30[+0]	1.55[+0]	1.77[+0]	2.14[+0]	2.37[+0]	2.64[+0]	1.70[+0]	2.90[−1]	5.39[−4]
1.6	1.92[−1]	5.42[−1]	6.47[−1]	7.42[−1]	8.98[−1]	9.97[−1]	1.10[+0]	7.09[−1]	1.24[−1]	2.63[−4]
1.7	7.84[−2]	2.17[−1]	2.60[−1]	2.99[−1]	3.60[−1]	3.98[−1]	4.30[−1]	2.72[−1]	4.93[−2]	1.36[−4]
1.8	3.14[−2]	8.34[−2]	1.01[−1]	1.16[−1]	1.38[−1]	1.51[−1]	1.58[−1]	9.72[−2]	1.86[−2]	7.38[−5]
M	69.0	81.0	90.0	96.0	104.0	105.0	91.0	59.0	19.0	0.0

TABLE IV. The time-dependent x-ray source measured from the rear of a 7500-Å Au foil. The units for the thermal part of the distribution, specified at energies in keV from 0.1 to 1.8, are J/keV ns into 4π. The units for the M band specified as M are J/ns into 4π. The times are in ns from 0.53 to 1.43. The notation used (3.38[−1]) represents 3.38×10^{-1}.

Energy (keV) \ Time (ns)	0.53	0.63	0.73	0.83	0.93	1.03	1.13	1.23	1.33	1.43
0.1	1.42[+1]	3.09[+1]	4.89[+1]	6.40[+1]	7.57[+1]	8.24[+1]	8.45[+1]	7.99[+1]	7.10[+1]	6.30[+1]
0.2	6.22[+1]	1.28[+2]	2.03[+2]	2.65[+2]	3.09[+2]	3.34[+2]	3.26[+2]	2.94[+2]	2.46[+2]	2.05[+2]
0.3	2.88[+1]	7.87[+1]	1.40[+2]	1.91[+2]	2.28[+2]	2.49[+2]	2.38[+2]	2.15[+2]	1.73[+2]	1.30[+2]
0.4	1.66[+1]	6.59[+1]	1.31[+2]	1.83[+2]	2.25[+2]	2.39[+2]	2.31[+2]	1.89[+2]	1.33[+2]	8.51[+1]
0.5	6.48[+0]	3.10[+1]	6.97[+1]	1.06[+2]	1.27[+2]	1.37[+2]	1.24[+2]	8.90[+1]	5.81[+1]	3.50[+1]
0.6	4.70[+0]	2.02[+1]	4.97[+1]	7.30[+1]	8.52[+1]	8.67[+1]	6.95[+1]	4.66[+1]	2.81[+1]	1.44[+1]
0.7	8.89[+0]	2.74[+1]	4.72[+1]	6.54[+1]	7.79[+1]	7.13[+1]	5.36[+1]	3.65[+1]	1.99[+1]	7.98[+0]
0.8	2.47[+1]	5.11[+1]	2.83[+1]	4.63[+1]	5.86[+1]	5.35[+1]	4.26[+1]	3.13[+1]	1.60[+1]	5.69[+0]
0.9	4.89[+1]	7.43[+1]	1.66[+1]	3.22[+1]	4.20[+1]	4.00[+1]	3.45[+1]	2.65[+1]	1.25[+1]	4.33[+0]
1.0	4.06[+1]	5.49[+1]	1.63[+1]	2.90[+1]	3.58[+1]	3.44[+1]	2.93[+1]	2.01[+1]	8.59[+0]	2.96[+0]
1.1	1.75[+1]	2.43[+1]	2.27[+1]	3.09[+1]	3.39[+1]	3.18[+1]	2.48[+1]	1.41[+1]	5.27[+0]	1.80[+0]
1.2	5.72[+0]	8.60[+0]	3.26[+1]	3.23[+1]	3.11[+1]	2.81[+1]	1.97[+1]	9.09[+0]	2.98[+0]	1.01[+0]
1.3	1.91[+0]	3.09[+0]	3.79[+1]	2.86[+1]	2.48[+1]	2.17[+1]	1.39[+1]	5.40[+0]	1.59[+0]	5.38[−1]
1.4	6.82[−1]	1.16[+0]	3.47[+1]	2.14[+1]	1.71[+1]	1.46[+1]	8.72[+0]	2.98[+0]	8.07[−1]	2.73[−1]
1.5	2.59[−1]	4.58[−1]	2.56[+1]	1.37[+1]	1.03[+1]	8.64[+0]	4.91[+0]	1.53[+0]	3.92[−1]	1.32[−1]
1.6	1.04[−1]	1.87[−1]	1.55[+1]	7.55[+0]	5.48[+0]	4.56[+0]	2.51[+0]	7.40[−1]	1.83[−1]	6.14[−2]
1.7	4.38[−2]	7.95[−2]	7.83[+0]	3.67[+0]	2.62[+0]	2.17[+0]	1.18[+0]	3.38[+0]	8.21[−2]	2.76[−2]
1.8	1.93[−2]	3.48[−2]	3.38[+0]	1.59[+0]	1.13[+0]	9.39[−1]	5.11[−1]	1.47[−1]	3.57[−2]	1.20[−2]
M	33.0	39.0	42.0	45.0	39.0	26.0	11.0	2.0	0.0	0.0

higher-energy N band occurs more rapidly than the fall of the lower-energy O band. The decay time for the O band for the 5000-Å case is $\sim 400 \pm 75$ ps, while the fall time for the N band is 200 ± 75 ps. In the case of Ref. [17], the decay times are roughly 400 ps, as observed from Fig. 12 of Ref. [17]. The differences between the flat-top laser pulse in the present work and the nearly Gaussian pulse in the work of Ref. [17] may contribute to the discrepancy, since the late-time existence of the higher-energy N bands will be closely related to the degree of energy deposition on the front surface. The flat-top pulse, which rapidly turns off, provides no source of hot plasma production at late time, while the O band, between 200 and 300 eV, is a dominant part of the thermal emission from the rear surface plasma.

VI. CONCLUSIONS

The experiments presented above successfully develop and quantify an x-ray source that can be used to volumetrically heat a sample without critical density surface effects, no direct laser-matter interactions, or any hydrodynamic interactions with the x-ray-producing plasma. Experiments have been carried out to insure that the sample heated with the x-ray source behaves in a predictable manner and that the sample is heated uniformly over areas on the order of 0.1×0.1 cm^2. These results were achieved by observing the x rays transmitted from the rear of Au foils and observing the transmitted x rays, and comparison with previous studies has been made.

As a result of these experiments, we are now closer to producing an experimental test bed for plasma spectroscopic studies of hot, dense matter without a reliance on radiation hydrodynamics code simulations for interpretation of the results. Experiments are now under way to determine the density and temperature of tamped samples which are volumetrically heated. Providing a rigorous test for the simulation of these experiments requires independent temperature, density, and spectral information—at a minimum. To provide these quantities in a geometry that is not compromised by extraneous physical constraints such as critical density surfaces, laser-induced parametric instabilities, or the hydrodynamics of the source is the next step in this series of experiments.

Since the measured source is of primary interest and can be used by others to produce simulations of volumetrically heated material, we provide in the Appendix a simple time-dependent representation of the source. In providing this source, we hope that we will relieve researchers of the need to perform laser-plasma simulations to obtain the x-ray source when one is actually interested in the x-ray heating of a sample.

Finally, we note that the above investigation has not been a study in the optimization of the x-ray heating of a sample. The primary goal was to quantify an x-ray source that could be used to heat samples to reasonable temperatures at high density. Further research is required to optimize the Au foil thickness so that the x-ray flux is maximized while maintaining the foil against burn-through.

APPENDIX: TIME- AND ENERGY-DEPENDENT FLUX

In Tables I–IV representative measurements of the x-ray flux emitted from the back of four different foil thicknesses are presented. In each case, the thermal spectral energy region and the high-energy band which covers from 2000 to 4000-eV— but is preferentially emitted in the Au M band from 2300 to 3500 eV—are given in one table. The thermal part of the spectrum is given as energy in keV versus intensity in J/keV ns into 4π for the various times in ns. The high-energy contribution is in unit of J/ns and is specified by an M in the table.

[1] See *Handbook of Plasma Physics*, edited by M. N. Rosenbluth and R. Z. Sagdeev (North-Holland, New York, 1991).

[2] C. DeMichelis and M. Mattioli, Nucl. Fusion **21**, 677 (1981).

[3] See, for example, W. C. Mead *et al.*, Phys. Fluids **26**, 2316 (1983) and references cited therein.

[4] P. K. Carroll and G. O'Sullivan, Phys. Rev. A **25**, 275 (1982); J. Opt. Soc. Am. **71**, 227 (1981); F. O'Neill *et al.*, in *X-Rays from Laser Plasmas*, edited by M. C. Richardson (SPIE, Bellingham, WA, 1988), Vol. 831, p. 230.

[5] P. G. Burkhalter, C. M. Dozier, and D. J. Nagel, Phys. Rev. A **15**, 700 (1977); A. Zigler *et al.*, Phys. Lett. **75A**, 343 (1980); J. F. Seely, C. M. Brown, and U. Feldman, At. Data Nucl. Data Tables **43**, 145 (1989) and references cited therein.

[6] S. J. Davidson *et al.*, Appl. Phys. Lett. **52**, 847 (1988) and other backlight references.

[7] M. D. Rosen *et al.*, Phys. Fluids **22**, 2020 (1979).

[8] P. Celliers and K. Eidmann, Phys. Rev. A **41**, 3270 (1990); H. Nishimura *et al.*, Phys. Fluids **26**, 1688 (1982); T. Mochizuki *et al.*, Phys. Rev. A **36**, 3279 (1987).

[9] R. Sigel *et al.*, Phys. Rev. Lett. **65**, 587 (1990) and references cited therein.

[10] Y. Kato, K. Mima, N. Miyanaga, S. Arinaga, Y. Kitagawa, M. Nakasuta, and C. Yamanaka, Phys. Rev. Lett. **53**, 1057 (1984); X. Deng, X. Liang, Z. Cheng, W. Yu, and R. Ma, Appl. Opt. **25**, 377 (1986).

[11] R. E. Turner *et al.* (unpublished).

[12] D. R. Kania, L. Pan, H. N. Kornblum, P. Bell, O. N. Landen, and P. Piancetta, Rev. Sci. Instrum. **61**, 2765 (1990).

[13] H. N. Kornblum, R. L. Kauffman, and J. A. Smith, Rev. Sci. Instrum. **57**, 2179 (1986).

[14] T. Kita, T. Harada, N. Nakana, and H. Kurada, Appl. Opt. **22**, 512 (1983); G. P. Kiehn, O. Willi, A. R. Damerell, and M. H. Key, *ibid.* **26**, 425 (1987).

[15] W. E. Behring, J. H. Underwood, C. M. Brown, U. Feldman, J. F. Seely, F. J. Marshall, and M. C. Richardson, Appl. Opt. **27**, 2762 (1988).

[16] N. Kaiser, J. Meyer-ter-Vehn, and R. Sigel, Phys. Fluids B **1**, 1747 (1989).

[17] H. Nishimura, H. Takabe, K. Kondo, T. Endo, H. Shiraga, K. Sugimoto, T. Nishikawa, Y. Kato, and S. Nakai, Phys. Rev. A **43**, 3073 (1991).

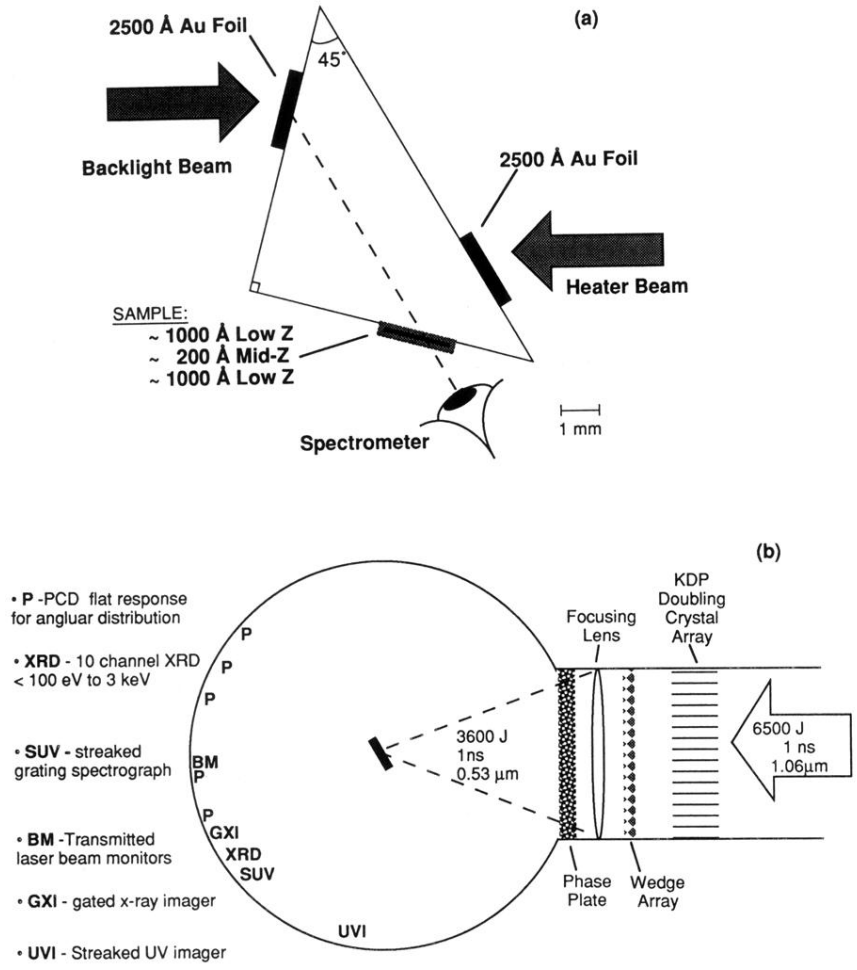

FIG. 1. (a) The schematic of an experimental design to allow quantitative analysis of the absorption spectrum. The key elements in the experiment are the backlight, the sandwiched sample, and a recording medium that allows the various sources to be measured at one time. (b) The experimental setup to measure the x-ray flux emitted from the rear side of a laser-irradiated gold foil. The position of the various diagnostics used in the experimental series is indicated.

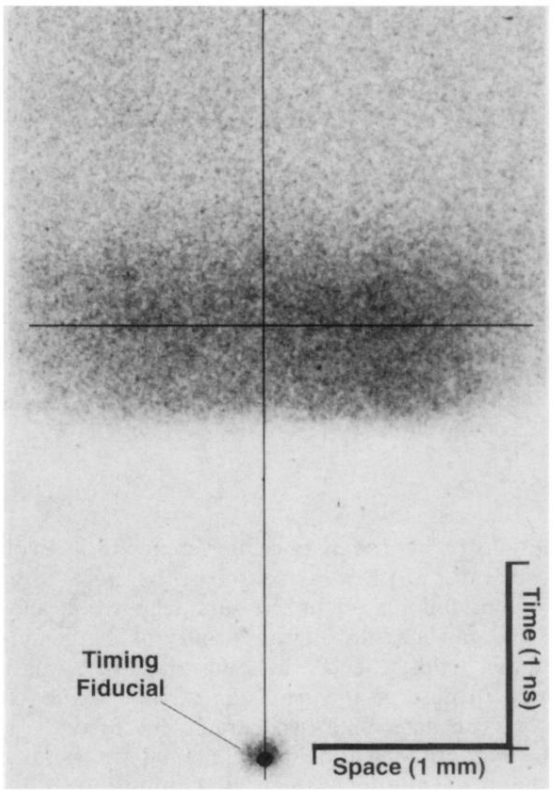

FIG. 10. The UV imaging streak camera record measuring the UV energy band around 3.1 eV. The spatial dimension is horizontal and the time axis is vertical. Note that the width of the transmitting region grows slightly in time. The vertical and horizontal lines indicate the positions where the curves presented in Fig. 11 are taken. The scale of the time and length axes is indicated by the bar in the lower right.

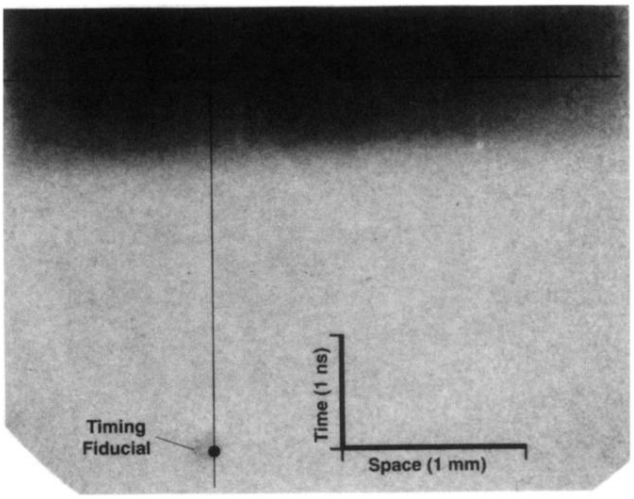

FIG. 12. The streaked UV image record with time in ns and space along an aluminum sample, placed as indicated in Fig. 1(a). The vertical and horizontal lines indicate the positions where the curves presented in Fig. 13 are taken. The scale of the time and length axes is indicated by the bar in the lower right.

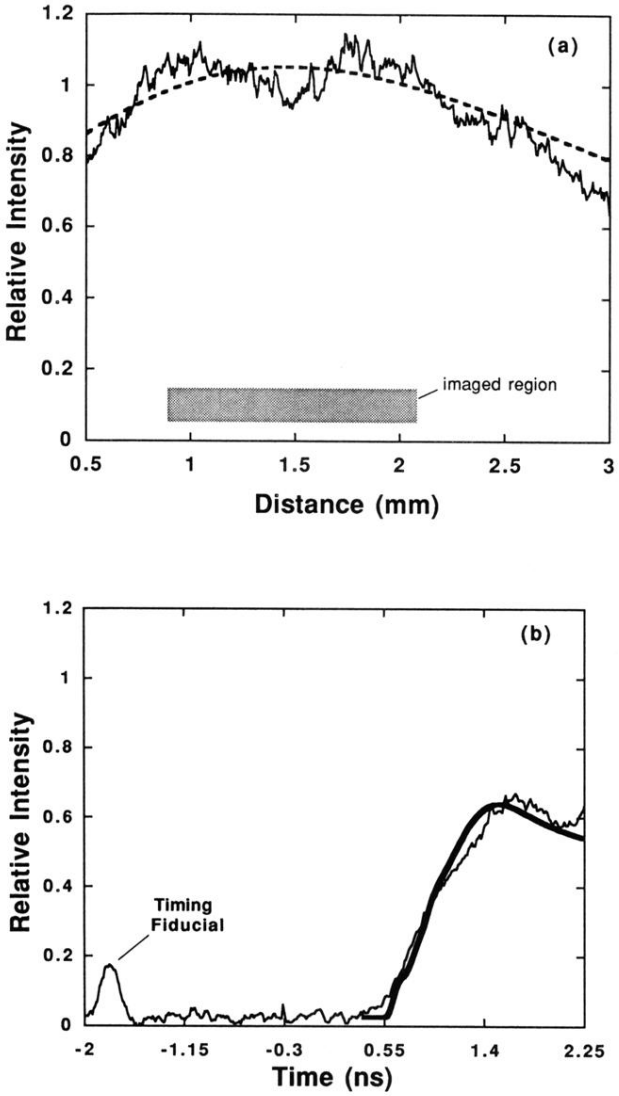

FIG. 13. Data along the lines indicated in Fig. 12. (a) The uniformity of the sample heating of the aluminum foil taken as the relative intensity of a horizontal line at time 0.2 ns vs the distance in mm along the target. The shaded region indicates the region of the sample that would be imaged in a full experimental configuration. The dotted line is a simple view factor calculation of the relative intensity across the sample given the known flux and the geometry. (b) The evolution of sample heating measured by taking a vertical line through the fiducial marker. The time is measured in ns and the ordinate is relative intensity. The thin line represents the data including the fiducial, while the thick line represents the simulation of the rear side emission of the aluminum plate.

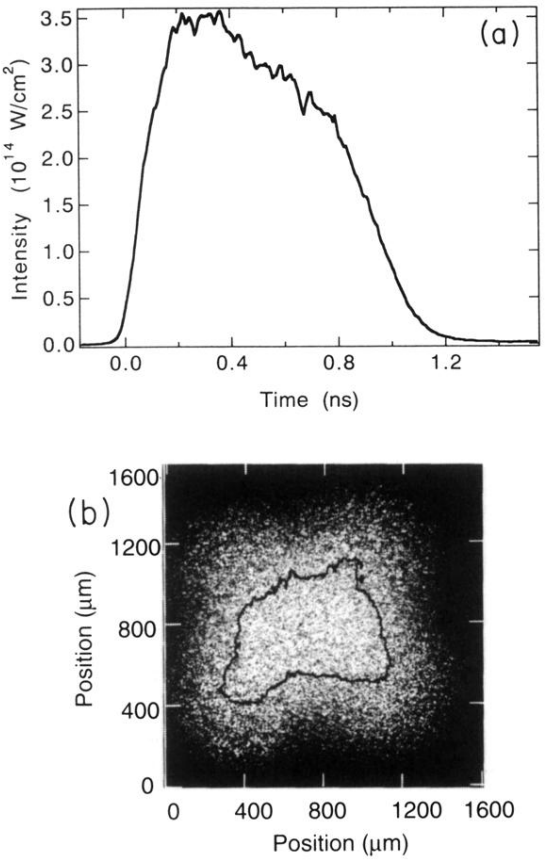

FIG. 2. (a) The Nova laser-beam temporal profile. The beam energy is shown in J/s vs the time in ns. (b) A two-dimensional image of the beam showing the intensity variation of the beam after the process of passing the beam through wedges and random phase plates. Both dimensions are measured in μm and a contour showing the region that is within 10% of the maximum, i.e., the 90% contour is indicated by the thick line.

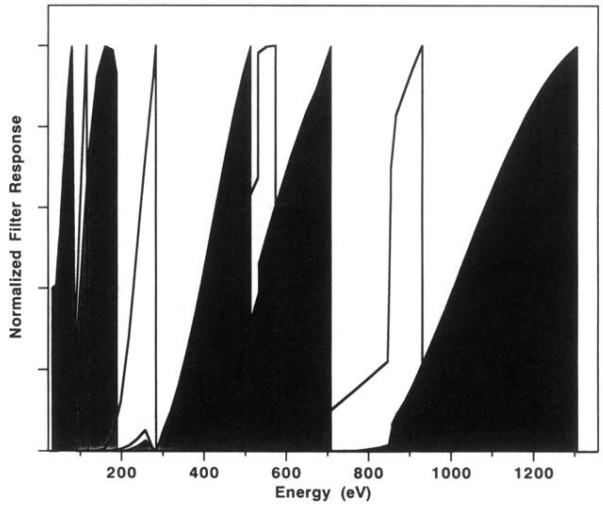

FIG. 3. The response curves for the FXRD channels used in the experimental series. The responses are normalized to a peak of unity for each channel. The energy scale is in eV.

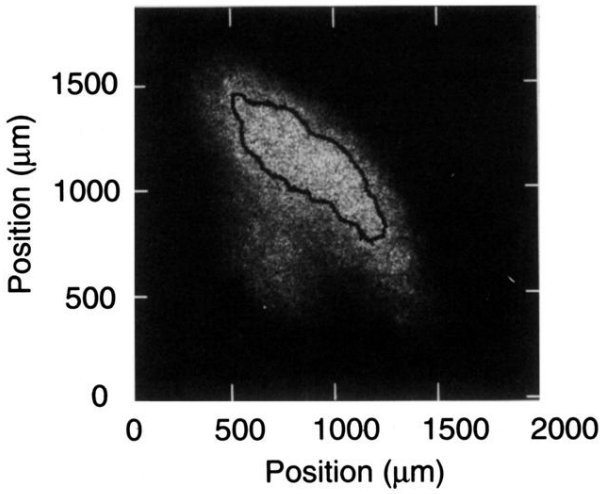

FIG. 9. The two-dimensional image of the rear side of the 2500-Å Au burn-through foil filtered to show the intensity of the energy band from 800 eV. The ordinate and the abscissa are measured in μm and this image is taken at 0.07 ns. As an indication of the intensity uniformity, the region of the x-ray foil that is within 10% of the maximum, i.e., the 90% contour, is shown on the image by the thick line.